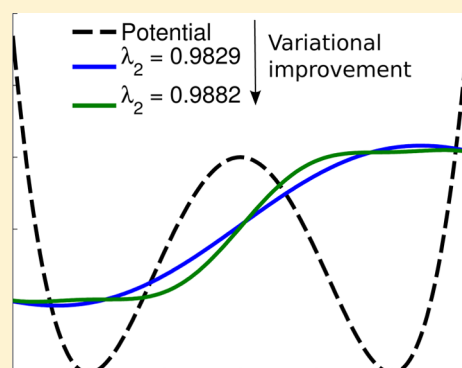


# Variational Approach to Molecular Kinetics

2 Feliks Nüske, Bettina G. Keller,\* Guillermo Pérez-Hernández, Antonia S. J. S. Mey, and Frank Noé\*

3 Department for Mathematics and Computer Science, Freie Universität of Berlin, 14195 Berlin, Germany

4 **ABSTRACT:** The eigenvalues and eigenvectors of the molecular dynamics  
5 propagator (or transfer operator) contain the essential information about the  
6 molecular thermodynamics and kinetics. This includes the stationary distribution,  
7 the metastable states, and state-to-state transition rates. Here, we present a  
8 variational approach for computing these dominant eigenvalues and eigenvectors.  
9 This approach is analogous the variational approach used for computing  
10 stationary states in quantum mechanics. A corresponding method of linear  
11 variation is formulated. It is shown that the matrices needed for the linear  
12 variation method are correlation matrices that can be estimated from simple MD  
13 simulations for a given basis set. The method proposed here is thus to first define  
14 a basis set able to capture the relevant conformational transitions, then compute the  
15 respective correlation matrices, and then to compute their dominant eigenvalues and  
16 eigenvectors, thus obtaining the key ingredients of the slow kinetics.



## 1. INTRODUCTION

17 Biomolecules, in particular proteins, often act as small but  
18 highly complex machines. Examples range from allosteric  
19 changes<sup>1,2</sup> to motor proteins, such as kinesin, which literally  
20 walks along microtubules,<sup>1,3</sup> and the ribosome, an enormous  
21 complex of RNA molecules and proteins responsible for the  
22 synthesis of proteins in the cell.<sup>1,4</sup> To understand how these  
23 biomolecular machines work, it does not suffice to know their  
24 structure, that is, their three-dimensional shape. One needs to  
25 understand how the structure gives rise to the particular  
26 conformational dynamics by which the function of the molecule  
27 is achieved. Protein folding is the second field of research in  
28 which conformational dynamics plays a major role. Proteins are  
29 long polymers of amino acids that fold into particular three-  
30 dimensional structure. The astonishingly efficient search for this  
31 native conformation in the vast conformational space of the  
32 protein can be understood in terms of its conformational  
33 dynamics. Besides time-resolved experiments, molecular dynamics  
34 simulations are the main technique to investigate conformational  
35 dynamics. To date, these simulations yield information on the  
36 structure and dynamics of biomolecules at a spatial and temporal  
37 resolution, which cannot be paralleled by any experimental  
38 technique. However, the extraction of kinetic models from  
39 simulation data is far from trivial, since kinetic information cannot  
40 be inferred from structural similarity.<sup>5,6</sup> Similar structures might be  
41 separated by large kinetic barriers, and structures that are far apart  
42 in some distance measure might be kinetically close.

43 A natural approach toward modeling the kinetics of molecules  
44 involves the partitioning of conformation space into discrete  
45 states.<sup>7–17</sup> Subsequently, transition rates or probabilities between  
46 states can be calculated, either based on rate theories,<sup>7,18,19</sup> or  
47 based on transitions observed in MD trajectories.<sup>6,13,15,16,20–22</sup> The  
48 resulting models are often called transition networks, Master  
49 equation models, or Markov (state) models (MSM),<sup>23–25</sup> where  
50 “Markovianity” means that the kinetics are modeled by a

memoryless jump process between states. In Markov state models, 51  
it is assumed that the molecular dynamics simulations used 52  
represent an ergodic, reversible, and metastable Markov process.<sup>25</sup> 53  
Ergodicity means that every possible state would be visited in an 54  
infinitely long trajectory and every initial probability distribution of 55  
the system converges to a Boltzmann distribution. Reversibility 56  
reflects the assumption that the system is in thermal equilibrium. 57  
Metastability means that there are parts of the state space in which 58  
the system remains over time scales much longer than the fastest 59  
fluctuations of the molecule. In order to construct an MSM, 60  
the conformational space of the molecule is discretized into 61  
nonoverlapping microstates, and the observed transitions between 62  
pairs of microstates are counted. One obtains a square matrix with 63  
transition probabilities, the so-called transition matrix, from which 64  
a wide range of kinetic and thermodynamic properties can be 65  
calculated. The equilibrium probability distribution (in the chosen 66  
state space) is obtained as the first eigenvector of the transition 67  
matrix. Directly from the matrix elements, one can infer kinetic 68  
networks and transition paths.<sup>26,27</sup> The dominant eigenvectors of 69  
the transition matrix are used to identify metastable states.<sup>28–32</sup> 70  
Each dominant eigenvector can be interpreted as a kinetic process, 71  
and the associated eigenvalue is related to the time scale on which 72  
this process occurs.<sup>25</sup> All this information can be combined to 73  
reconstruct the hierarchical structure of the energy landscape.<sup>31,33</sup> 74  
Finally, transition matrices represent a very useful framework to 75  
connect data from time-resolved experiments with simulation 76  
data.<sup>34,35</sup> Over the past decade, extensive knowledge on which 77  
factors determine the quality of an MSM has been accumulated. 78  
For example, MSMs that are constructed using the internal 79  
degrees of freedom of the molecule tend to yield better results 80  
than those that were constructed using global descriptors of 81  
the structure (H-bond patterns, number of native contacts).<sup>31</sup> 82

Received: October 21, 2013

83 Also, degrees of freedom that are not included in the model should  
84 decorrelate on short time scales from those that are included.<sup>36</sup>  
85 Naturally, the sampling of the transitions limits the accuracy of an  
86 MSM, and tools to account for this error have been  
87 developed.<sup>37–39</sup> On the whole, the research field has matured to  
88 a point at which well-tested protocols for the construction of  
89 MSMs from MD data have been established,<sup>25,40,41</sup> and software  
90 to construct and validate Markov state models from MD data is  
91 freely available.<sup>42,43</sup> MSMs have been applied to analyze the  
92 conformational dynamics of peptides<sup>5,31,44</sup> and of small protein  
93 domains, such as Villin head piece,<sup>45</sup> pin WW,<sup>46</sup> FiP35 WW,<sup>45</sup>  
94 Recently, it has become possible to analyze the folding  
95 equilibria of full fast-folding proteins.<sup>47–49</sup> MSMs have also  
96 been used to investigate conformational changes, such as the  
97 self-association step in the maturation of HIV-protease,<sup>50</sup>  
98 ligand binding,<sup>51</sup> or the oligomerization of peptide fragments  
99 into amyloid structures.<sup>52</sup>

100 An important aspect that has limited the routine use of  
101 MSMs is the difficulty to obtain a state space discretization that  
102 will give rise to an MSM that precisely captures the slow  
103 kinetics. The high-dimensional molecular space is usually first  
104 discretized using clustering methods in some metric space. The  
105 form and location of these clusters, sometimes called “MSM  
106 microstates”, are crucial for determining the quality of the  
107 estimated transition rates.<sup>53–55</sup> Various metrics and clustering  
108 methods have been attempted for different molecular systems.  
109 Small peptides can be well described by a direct discretization  
110 of their backbone dihedrals.<sup>31</sup> It was suggested in ref 56 to use a  
111 dihedral principal component analysis to reduce the dihedral  
112 space to a low-dimensional subspace and subsequently cluster  
113 this space using, for example, *k*-means. A rather general metric  
114 is the pairwise minimal RMSD-metric in conjunction with some  
115 clustering method, such as *k*-centers or *k*-medoids.<sup>25,30,41</sup>  
116 Recently, the time-lagged independent component analysis  
117 (TICA) method was put forward, a dimension reduction  
118 approach in which a “slow” low-dimensional subspace is  
119 identified, which has been shown to provide improved MSMs  
120 over previously employed metrics.<sup>57,58</sup>

121 In recent years, it has been established that the precision of  
122 an MSM depends on how well the discretization approximates  
123 the shape of the eigenfunction of the underlying dynamical  
124 operator (propagator or transfer operator) of the dynamics.<sup>55</sup>  
125 When the dynamics are metastable, these eigenfunctions will be  
126 almost constant on the metastable states, and change rapidly at  
127 the transition states.<sup>59</sup> Thus, methods that have sought to construct  
128 a maximally metastable discretization<sup>30,60</sup> have been relatively  
129 successful for metastable dynamics. However, the MSM can be  
130 improved by using a nonmetastable discretization, especially when  
131 it finely discretizes the transition states, so as to trace the variation  
132 of the eigenfunction in these regions.<sup>25,55</sup> An alternative way of  
133 achieving a good resolution at the transition state without using a  
134 fine discretization is to use appropriately placed smooth basis  
135 functions, such as the smooth partition-of-unity basis functions  
136 suggested in refs 61–63. The core-based discretization method  
137 proposed in ref 11 effectively employs a smooth partition-of-unity  
138 basis defined by the committor functions between sets.<sup>64</sup>

139 All of the above methods have in common that they attempt  
140 to construct an appropriate discretization based on the  
141 simulation data. This has a two-fold disadvantage: (1) different  
142 simulation runs will produce different discretizations, making  
143 them hard to compare; (2) data-based clusters have no intrinsic  
144 meaning. Interpretation in terms of structural transitions must  
145 be recovered by analyzing the molecular configurations

146 contained in specific clusters. With all of the above methods,  
147 choosing an appropriate combination of the metric, the  
148 clustering method, and the number and the location of clusters  
149 or cores is still often a trial-and-error approach.

150 Following the recently introduced variational principle for  
151 metastable stochastic processes,<sup>65</sup> we propose a variational  
152 approach to molecular kinetics. Starting from the fact that  
153 the molecular dynamics propagator is a self-adjoint operator,  
154 we can formulate a variational principle. Using the method of  
155 linear variation we derive a Roothaan–Hall-type generalized  
156 eigenvalue problem that yields an optimal representation of  
157 eigenvectors of the propagator in terms of an arbitrary basis  
158 set. Both ordinary MSMs using crisp clustering and MSMs  
159 with a smooth discretization can be understood as special  
160 cases of this variational approach. In contrast to previous  
161 MSMs using smooth discretization, our basis functions do not  
162 need to be a partition of unity, although this choice has  
163 some merits.

164 Besides its theoretical attractiveness, the variational approach  
165 has some advantages over MSMs. First, the data-driven  
166 discretization is replaced by a user-selection of an appropriate  
167 basis set, typically of internal molecular coordinates. The  
168 chosen basis set may reflect chemical intuition—for example,  
169 basis functions may be predefined to fit known transition states  
170 of backbone dihedral angles or formation/dissociation of  
171 tertiary contacts between hydrophobically or electrostatically  
172 interacting groups. As a result, one may obtain a precise model  
173 with fewer basis functions needed than discrete MSM states.  
174 Moreover, each basis function is associated with a chemical  
175 meaning, and thus, the interpretation of the estimated  
176 eigenfunctions becomes much more straightforward than for  
177 MSMs. When using the same basis set for different molecular  
178 systems of the same class, one obtains models that are directly  
179 comparable in contrast to conventional MSMs. The represen-  
180 tation of the propagator eigenfunctions can still be systemati-  
181 cally improved by adding more basis functions or by varying the  
182 basis set.

183 Our method is analogous to the method of linear variation  
184 used in quantum chemistry.<sup>66</sup> The major difference is that the  
185 propagator is self-adjoint with respect to a non-Euclidean scalar  
186 product, whereas the Hamiltonian is self-adjoint with respect to  
187 the Euclidean scalar product. The derivation of the method is  
188 detailed in section 2 and Appendices A–C.

## 2. THEORY

2.1. **Dynamical Propagator.** Consider the conformational  
189 space  $X$  of an arbitrary molecule consisting of  $N$  atoms, that is,  
190 the  $3N-6$ -dimensional space spanned by the internal degrees of  
191 freedom of the molecule. The conformational dynamics of the  
192 molecule in this space can be represented by a dynamical  
193 process  $\{x_t\}$ , which samples at a given time  $t$  a particular point  
194  $x_t \in X$ . In this context,  $x_t$  is often called a trajectory. This  
195 process is governed by the equations of motion, and it can be  
196 simulated using standard molecular-dynamics programs. We  
197 assume that an implementation of thermostatted molecular  
198 dynamics is employed, which ensures that  $x_t$  is time-  
199 homogeneous, Markovian, ergodic, and reversible with respect  
200 to a unique stationary density (usually the Boltzmann  
201 distribution). We introduce a propagator formulation of these  
202 dynamics, following.<sup>65</sup> Readers familiar with this approach might  
203 want to skip to section 2.2.  
204

205 Next, consider an infinite ensemble of molecules of the same  
206 type, distributed in the conformational space according to some

207 initial probability density  $\rho_0(x)$ . This initial probability density  
 208 evolves in time in a definite manner that is determined by the  
 209 aforementioned equations of motion for the individual  
 210 molecules. We assume that the time evolution is Markovian

$$p(x, y; \tau) dy = \mathbb{P}(x_{t+\tau} \in y dy | x_t = x) \quad (1)$$

$$= \mathbb{P}(x_t \in y dy | x_0 = x) \quad (2)$$

211 where  $\tau$  is a finite time step, and  $p(x, y; \tau)$  is the so-called  
 212 transition density, which is assumed to be independent of time  
 213  $t$  (time-homogeneous). Figure 1 shows an example of the

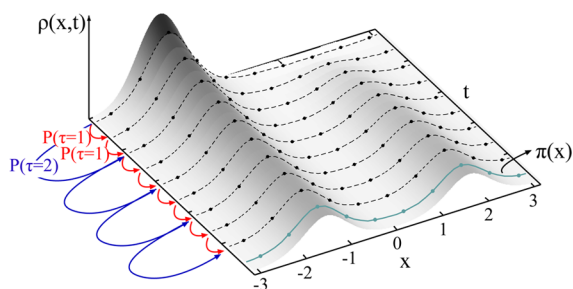


**Figure 1.** Illustration of two propagators acting on a probability density  $\rho_i(x)$ . Gray surface: time evolution of  $\rho_i(x)$ . Black dotted line: snapshots of  $\rho_i(x)$ . Cyan line: equilibrium density  $\pi(x)$  to which  $\rho_i(x)$  eventually converges. Red, blue: propagators with different lag times  $\tau$ , which propagate an initial density by a time step  $\tau$  in time.

214 time-evolution of a probability density in a one-dimensional  
 215 two-well potential. Equation 2 implies that the probability of  
 216 finding a molecule in conformation  $y$   $dy$  at time  $t + \tau$  depends  
 217 only on the conformation  $x$  it has occupied one time step  
 218 earlier, and not on the sequence of conformations it has visited  
 219 before  $t$ . The unconditional probability density of finding a  
 220 molecule in conformation  $y$  at time  $t + \tau$  is obtained by  
 221 integrating over all starting conformations  $x$

$$\rho_{t+\tau}(y) = \int_X p(x, y; \tau) \rho_t(x) dx \quad (3)$$

223 This equation, in fact, defines an operator  $\mathcal{P}(\tau)$  that propagates  
 224 the probability density by a finite time step  $\tau$

$$\rho_{t+\tau}(x) = \mathcal{P}(\tau) \rho_t(x) \quad (4)$$

$$\rho_{t+n\tau}(x) = \mathcal{P}^n(\tau) \rho_t(x) \quad (5)$$

$\mathcal{P}(\tau)$  is called a propagator, and the time step  $\tau$  is often called  
 227 the lag time of the propagator. One says the propagator is  
 228 parametrized with  $\tau$ . Such as  $p(x, y; \tau)$ , the propagator  $\mathcal{P}(\tau)$  in  
 229 eq 5 is time-homogeneous; that is, it does not depend on  $t$ . The  
 230 way it acts on a density  $\rho(x, t)$  is not a function of the time  $t$  at  
 231 which this density occurs but only a function of the time step  $\tau$   
 232 by which the density is propagated (Figure 1).

233 The way the propagator acts on the density can be  
 234 understood in terms of its eigenfunctions  $\{l_\alpha(x)\}$  and  
 235 associated eigenvalues  $\{\lambda_\alpha\}$ , which are defined by the following  
 236 eigenvalue equation

$$\mathcal{P}(\tau) l_\alpha(x) = \lambda_\alpha l_\alpha(x) \quad (6)$$

238 For the class of processes which are discussed in this  
 239 publication, the eigenfunctions form a complete set of  $\mathbb{R}^{3N}$ .  
 240 Hence, any probability density (in fact any function) in this

space can be expressed as linear combination of  $\{l_\alpha(x)\}$ .  
 Equation 5 can be rewritten as

$$|\rho_{t+n\tau}(x)\rangle = \sum_\alpha c_\alpha \lambda_\alpha^n |l_\alpha(x)\rangle \quad (7)$$

$$= \sum_\alpha c_\alpha e^{-n\tau/t_\alpha} |l_\alpha(x)\rangle \quad (8)$$

where  $n$  is the number of discrete time steps  $\tau$ . The  
 eigenfunctions can be interpreted as kinetic processes that  
 transport probability density from one part of the conforma-  
 tional space to another and thus modulate the shape of the  
 overall probability density. See ref 25 for a detailed explanation  
 of the interpretation of eigenfunctions. The eigenvalues are  
 linked to the time scales  $t_\alpha$  on which the associated kinetic  
 processes take place by

$$t_\alpha = -\frac{\tau}{\ln(\lambda_\alpha)} \quad (9)$$

These time scales are of particular interest because they may  
 be accessible using various kinetic experiments.<sup>35,67–69</sup>

Given the aforementioned properties of the molecular  
 dynamics implementation,  $\mathcal{P}(\tau)$  is an operator with the  
 following properties. A more detailed explanation can be  
 found in Appendix A.

- $\mathcal{P}(\tau)$  has a unique stationary density; that is, there is a  
 unique solution  $|\pi(x)\rangle$  to the eigenvalue problem  
 $\mathcal{P}(\tau)|\pi(x)\rangle = |\pi(x)\rangle$ .
- Its eigenvalue spectrum is bounded from above by  $\lambda_1 = 1$ .  
 Also,  $\lambda_1$  is the only eigenvalue of absolute value equal  
 to one.
- $\mathcal{P}(\tau)$  is self-adjoint with respect to the weighted scalar  
 product  $\langle fg \rangle_{\pi^{-1}} = \int_\Omega f(x)g(x)\pi^{-1}(x)dx$ . Consequently,  
 its eigenfunctions  $|l_\alpha(x)\rangle$  form an orthonormal basis of the  
 Hilbert space of square-integrable functions with respect  
 to this scalar product. Its eigenvalues are real and can be  
 numbered in descending order:

$$1 = \lambda_1 > \lambda_2 \geq \lambda_3 \geq \dots \quad (10)$$

**2.2. Variational Principle and the Method of Linear  
 Variation.** A variational principle can be derived for any  
 operator whose eigenvalue spectrum is bound (either from  
 above or from below) and whose eigenvectors form a complete  
 basis set and are orthonormal with respect to a given scalar  
 product. The variational principle for propagators was derived in.<sup>65</sup>  
 The derivation is analogous to the derivation of the variational  
 principle of the quantum-mechanical Hamilton operator.<sup>66</sup> For  
 convenience, we give a compact derivation in Appendix B.

The variational principle can be summarized in three steps. First,  
 for the exact eigenfunction  $|l_\alpha(x)\rangle$ , the following equality holds:

$$\langle l_\alpha | \mathcal{P}(\tau) | l_\alpha \rangle_{\pi^{-1}} = \lambda_\alpha(\tau) = e^{-\tau/t_\alpha} \quad (11)$$

The expression  $\langle f | \mathcal{P}(\tau) | f \rangle_{\pi^{-1}}$  is the analogue of the quantum-  
 mechanical expectation value and has the interpretation of a time-  
 lagged autocorrelation (c.f. section 2.3). The autocorrelation of the  
 $\alpha$ -th eigenfunction is identical to the  $\alpha$ -th eigenvalue.

Second, for any trial function  $|f\rangle$  that is normalized according  
 to eq 64, the following inequality holds:

$$\langle f | \mathcal{P}(\tau) | f \rangle_{\pi^{-1}} = \int_X f(x)\pi^{-1}(x)\mathcal{P}(\tau)f(x)dx \quad (12)$$

$$\leq \lambda_1 = 1 \quad (13)$$



where equality  $\langle f|\mathcal{P}(\tau)|f\rangle_{\pi^{-1}} = \lambda_1$  is achieved if and only if  $|f\rangle = |\lambda_1\rangle$ . This is at the heart of the variational principle.

Third, this inequality is applicable to other eigenfunctions: When  $|f\rangle$  is orthogonal to the  $\alpha - 1$  eigenfunctions, the variational principle will apply to the  $\alpha$ -th eigenfunction/eigenvalue pair:

$$\langle f|\mathcal{P}(\tau)|f\rangle_{\pi^{-1}} \leq \lambda_\alpha \quad (14)$$

$$\langle f|\lambda_\beta\rangle_{\pi^{-1}} = 0 \quad \forall \beta = 1, \dots, \alpha - 1 \quad (15)$$

This variational principle allows to formulate the method of linear variation for the propagator. Again, the derivation detailed in ref 65 is analogous to the derivation of the method of linear variation in quantum chemistry.<sup>66</sup> The trial function  $|f\rangle$  is linearly expanded using a basis of  $n$  basis functions  $\{|\varphi_i\rangle\}_{i=1}^n$

$$f = \sum_{i=1}^n a_i |\varphi_i\rangle \quad (16)$$

where  $a_i$  are the expansion coefficients. We only choose basis sets consisting of real-valued functions because all eigenvectors of  $\mathcal{P}(\tau)$  are real-valued functions. Consequently, the expansion coefficients  $a_i$  are real numbers. However, the basis set does not necessarily have to be orthonormal. In the method of linear variation, the expansion coefficients  $a_i$  are varied such that the right-hand side of eq 13 becomes maximal, while the basis functions are kept constant. The variation is carried out under the constraint that  $|f\rangle$  remains normalized with respect to eq 64 using the method of Lagrange multipliers. For details, see Appendix C. The derivation leads to a matrix formulation of eq 6:

$$\mathbf{C}\mathbf{a} = \lambda\mathbf{S}\mathbf{a} \quad (17)$$

$\mathbf{a}$  is the vector of expansion coefficients  $a_i$ ,  $\mathbf{C}$  is the (time-lagged) correlation matrix with elements

$$C_{ij} = \langle \varphi_i|\mathcal{P}(\tau)|\varphi_j\rangle_{\pi^{-1}} \quad (18)$$

and  $\mathbf{S}$  is the overlap matrix of the basis set, where the overlap is calculated with respect to the weighted scalar product

$$S_{ij} = \langle \varphi_i|\varphi_j\rangle_{\pi^{-1}} \quad (19)$$

Solving the generalized eigenvalue problem in eq 17, one obtains the first  $n$  eigenvectors of  $\mathcal{P}(\tau)$  expressed in the basis  $\{|\varphi_i\rangle\}_{i=1}^n$  and the associated eigenvalues  $\lambda_\alpha$ .

**2.3. Estimating the Matrix Elements.** To solve the generalized eigenvalue equation (eq 17), we need to calculate the matrix elements  $C_{ij}$ . In the quantum chemical version of the linear variation approach, the matrix elements  $H_{ij}$  for the Hamiltonian  $\mathcal{H}$  (see Appendix A) are calculated directly with respect to the chosen basis, either analytically or by solving the integral  $H_{ij} = \langle \varphi_i|\mathcal{H}|\varphi_j\rangle$  numerically. Such a direct treatment is not possible for the matrix elements of the propagator. However, we can use a trajectory  $x_t$  of a single molecule, as it is generated for example by MD simulations, to sample the matrix elements and thus obtain an estimate for  $C_{ij}$ . For this, we introduce a basis set  $\{\chi_i\}$  consisting of the  $n$  cofunctions of the original basis set  $\{\varphi_i\}$  by weighting the original functions with  $\pi^{-1}$

$$\chi_i(x) = \pi^{-1}(x)\varphi_i(x) \Leftrightarrow \varphi_i = \pi(x)\chi_i(x) \quad (20)$$

Inserting eq 20 into the definition of the matrix elements  $C_{ij}$  (eq 18), we obtain

$$\begin{aligned} C_{ij} &= \langle \varphi_i|\mathcal{P}(\tau)|\varphi_j\rangle_{\pi^{-1}} \\ &= \langle \chi_i|\pi|\mathcal{P}(\tau)|\pi\chi_j\rangle_{\pi^{-1}} \\ &= \int_X \int_X \chi_i(z)p(y, z, \tau)\pi(y)\chi_j(y)dy dz \end{aligned} \quad (21)$$

The last line of eq 21 has the interpretation of a time-lagged cross-correlation between the functions  $\chi_i$  and  $\chi_j$

$$\begin{aligned} \text{cor}(\chi_i, \chi_j, \tau) &:= \int_X \int_X \chi_i(z)\mathbb{P}(x_{t+\tau} = z|x_t = y) \\ &\quad \times \chi_j(y)\mathbb{P}(x_t = y)dy dz \end{aligned} \quad (22)$$

which can be estimated from a time-continuous time series  $x_t$  of length  $T$  as

$$\widehat{\text{cor}}_T(\chi_i, \chi_j, \tau) = \frac{1}{T-\tau} \int_0^{T-\tau} \chi_j(x_t)\chi_i(x_{t+\tau})dt \quad (24)$$

or from a time-discretized time series  $x_t$  as

$$\widehat{\text{cor}}_T(\chi_i, \chi_j, \tau) = \frac{1}{N_T - n_\tau} \sum_{i=1}^{N_T - n_\tau} \chi_j(x_i)\chi_i(x_{i+n_\tau}) \quad (25)$$

where  $N_T = T/\Delta t$ ,  $n_\tau = \tau/\Delta t$ , and  $\Delta t$  is the time step of the time-discretized time series. In the limit of infinite sampling and for an ergodic process, the estimate approaches the true value

$$C_{ij} = \text{cor}(\chi_i, \chi_j, \tau) = \lim_{T \rightarrow \infty} \widehat{\text{cor}}_T(\chi_i, \chi_j, \tau) \quad (26)$$

Note that the second line in eq 21 can also be read as the matrix representation of an operator which acts on the space spanned by  $\{\chi_i\}$ , the cofunctions of  $\{\varphi_i\}$  (eq 20). This is the so-called transfer operator  $\mathcal{J}(\tau)$ .

$$C_{ij}(\tau) = \langle \chi_i|\mathcal{P}(\tau)|\pi\chi_j\rangle_{\pi^{-1}} \quad (27)$$

$$= \langle \chi_i|\mathcal{J}(\tau)|\chi_j\rangle_{\pi} \quad (28)$$

$$= \langle \chi_i|\mathcal{J}(\tau)|\chi_j\rangle_{\pi} \quad (28)$$

with

$$\mathcal{J}(\tau)|f(z)\rangle = \frac{1}{\pi(z)} \int_X p(y, z, \tau)\pi(y)f(y)dy \quad (29)$$

In particular,  $\mathcal{J}(\tau)$  has the same eigenvalues as the propagator and its eigenfunctions are the cofunctions of the propagator eigenfunctions:

$$r_\alpha(x) = \pi^{-1}(x)l_\alpha(x) \quad (30)$$

We will sometimes refer to the functions  $r_\alpha$  as right eigenfunctions. For more details on the transfer operator the reader is referred to ref 59.

**2.4. Crisp Basis Sets—Conventional MSMs.** Markov state models (MSMs), as they have been discussed up to now in the literature,<sup>23–25,28,30,31,40–43,55,70</sup> arise as a special case of the proposed method. Namely, the choice of basis sets in conventional MSMs is restricted to indicator functions, that is, functions that have the value 1 on a particular set  $S_i$  of the conformational space  $X$  and the value 0 otherwise

$$\chi_i^{\text{MSM}}(x) = \begin{cases} 1 & \text{if } x \in S_i \\ 0 & \text{otherwise} \end{cases} \quad (31)$$

373 In effect, this is a discretization of the conformational space,  
374 for which the estimation of the matrix  $\mathbf{C}$  (eq 25) reduces to  
375 counting the observed transitions  $z_{ij}$  between sets  $S_i$  and  $S_j$

$$C_{ij} = \frac{1}{N_T - n_\tau} \sum_{t=1}^{N_T - n_\tau} \chi_j^{\text{MSM}}(x_t) \chi_i^{\text{MSM}}(x_{t+n_\tau}) \quad (32)$$

$$= \frac{z_{ij}}{N_T - n_\tau} \quad (33)$$

376 It is easy to verify,<sup>65</sup> that the overlap matrix  $\mathbf{S}$  is a diagonal  
377 matrix, with entries  $\pi_i$  equal to the stationary probabilities of the  
378 sets:

$$S_{ii} = \int_{S_i} \pi(x) dx = : \pi_i \quad (34)$$

380 Thus, the eigenvalue problem eq 17 becomes

$$\mathbf{C}\mathbf{a} = \lambda \mathbf{\Pi}\mathbf{a} \quad (35)$$

$$\mathbf{T}\mathbf{a} = \lambda \mathbf{a} \quad (36)$$

383 where  $\mathbf{C}$  is the correlation matrix,  $\mathbf{\Pi} = \mathbf{S} = \text{diag}\{\pi_1, \dots, \pi_n\}$  is the  
384 diagonal matrix of stationary probabilities, and  $\mathbf{T} = \mathbf{\Pi}^{-1}\mathbf{C}$  is the  
385 MSM transition matrix. Thus,  $\mathbf{a}$  is a right eigenvector of  
386 the MSM transition matrix. As the equations above provide the  
387 linear variation optimum, using MSMs and their eigenvectors  
388 corresponds to finding an optimal step-function approximation  
389 of the eigenfunctions. Moreover, we can use the weighted  
390 functions

$$\mathbf{b}_\alpha = \mathbf{\Pi}\mathbf{a}_\alpha \quad (37)$$

392 and see that they are left eigenfunctions of  $\mathbf{T}$ :

$$\mathbf{T}\mathbf{\Pi}^{-1}\mathbf{b} = \lambda \mathbf{\Pi}^{-1}\mathbf{b} \quad (38)$$

$$\mathbf{b}^T \mathbf{\Pi}^{-1} \mathbf{C} = \lambda \mathbf{b}^T \quad (39)$$

$$\mathbf{b}^T \mathbf{T} = \lambda \mathbf{b}^T \quad (40)$$

396 Note that the crisp basis functions form a partition of unity,  
397 meaning that their sum is the constant function with value one,  
398 which is the first exact eigenfunction of the transfer operator  $\mathcal{J}$   
399 ( $\tau$ ). For this reason, any state space partition that is a partition  
400 of unity solves the approximation problem of the first  
401 eigenvalue/eigenvector pair exactly: the first eigenvalue is  
402 exactly  $\lambda_1 = 1$ , the expansion coefficients  $a_i^1$  of the first  
403 eigenvector  $|r_1\rangle$  are all equal to one. The corresponding first left  
404 eigenvector  $\mathbf{b}_1 = \mathbf{\Pi}\mathbf{a}_1$  fulfills the stationarity condition:

$$\mathbf{b}_1^T = \mathbf{b}_1^T \mathbf{T} \quad (41)$$

406 and is, therefore, when normalized to an element sum of 1, the  
407 stationary distribution  $\pi$  of  $\mathbf{T}$ .

408 **2.5. Stationary Probability Distribution in the Variational Approach.** All previous MSM approaches—including  
409 the most common “crisp” cluster MSMs but also the smooth  
410 basis function approaches used in refs 24, 61, and 64—have  
411 directly or indirectly used basis functions that are a partition of  
412 unity. The reason for this is that using such a partition of unity,  
413 one can recover the exact first eigenvector and, thus, a  
414 meaningful stationary distribution.

416 In the present contribution, we give up the partition of unity  
417 condition, in order to be able to fully exploit the variational  
418 principle of the propagator with an arbitrary choice of basis sets.  
419 Therefore, we must investigate whether this approach is still

meaningful and can give us “something” like the stationary  
distribution.

Revisiting the MSM case, the stationary probability numbers  
 $\pi_i$  can be interpreted as stationary probabilities of the sets  $S_i$ , or,  
in other words, they measure the contribution of these sets to  
the full partition function  $Z$ :

$$\pi_i = \frac{Z_i}{Z} \quad (42)$$

$$Z_i = \int_{S_i} e^{-v(x)} dx = \int_X \chi_i^{\text{MSM}}(x) e^{-v(x)} dx \quad (43)$$

$$\sum_i \pi_i = \sum_i \frac{Z_i}{Z} = 1 \quad (44)$$

where  $v(x)$  is a reduced potential.

If we move on to a general basis, we can maintain a similar  
interpretation of the vector  $\mathbf{b}_1 = \mathbf{S}\mathbf{a}_1$ , as long as the first estimated  
eigenvalue  $\lambda_1$  remains equal to one. If we use the general definition  
of  $Z_i$  as the local density of the basis function  $\chi_i$ :

$$Z_i = \int_X \chi_i(x) e^{-v(x)} dx \quad (45)$$

Then, we still have

$$b_i = \frac{Z_i}{C} \quad (46)$$

for all  $i$ , where

$$C = \int_X \sum_i \chi_i(x) e^{-v(x)} dx \quad (47)$$

Interestingly, this relation also becomes approximately true if  
the estimated eigenvalue  $\lambda_1$  approaches one, as proved in  
Appendix D. As a result, the concept of the stationary  
distribution is still meaningful for basis sets that do not form  
a partition of unity. Moreover, it is completely consistent with  
the variational principle, because the vector  $\mathbf{b}_1$  becomes a  
probability distribution in the optimum  $\lambda_1 = 1$ .

**2.6. Estimation Method.** We summarize by formulating a  
computational method to estimate the eigenvectors and  
eigenvalues of the associated propagator from a time series  
(trajectory)  $x_t$  using an arbitrary basis set.

1. Choose a basis set  $\{\chi_i\}$ .
2. Estimate the matrix elements of the correlation matrix  $\mathbf{C}$   
and of the overlap matrix  $\mathbf{S}$  using eq 25 with lag times  $\tau$   
and 0, respectively.
3. Solve the generalized eigenvalue problem in eq 17. This  
yields the  $\alpha$ -th eigenvalue  $\lambda_\alpha$  of the propagator (and the  
transfer operator) and the expansion coefficients  $a_i^\alpha$  of  
the associated eigenvector.
4. The eigenvectors of the transfer operator are obtained  
directly from the expansion coefficients  $a_i^\alpha$  via

$$r_\alpha = \sum_{i=1}^n a_i^\alpha |\chi_i\rangle \quad (48)$$

5. If an estimate of the stationary density  $\pi$  is available, the  
eigenvectors of the propagator  $\mathcal{P}(\tau)$  are obtained from

$$l_\alpha = \sum_{i=1}^n a_i^\alpha |\varphi_i\rangle = \sum_{i=1}^n a_i^\alpha |\pi \chi_i\rangle \quad (49)$$

## 3. METHODS

464 **3.1. One-Dimensional Diffusion Models.** 3.1.1. *Simu-*  
 465 *lations.* We first consider two examples of one-dimensional  
 466 diffusion processes  $x_t$  governed by Brownian dynamics. The  
 467 process is then described by the stochastic differential equation

$$468 \quad dx_t = -\nabla v(x_t)dt + \sqrt{2D} dB_t \quad (50)$$

469 where  $v$  is the reduced potential energy (measured in units of  
 470  $k_B T$ , where  $k_B$  is the Boltzmann constant and  $T$  is the  
 471 temperature),  $D$  is the diffusion constant, and  $dB_t$  denotes the  
 472 differential of Brownian motion. For simplicity, we set all of the  
 473 above constants equal to one. The potential function is given by  
 474 the harmonic potential

$$475 \quad v(x) = 0.5x^2, \quad x \in \mathbb{R} \quad (51)$$

476 in the first case, and by the periodic double-well potential

$$477 \quad v(x) = 1 + \cos(2x), \quad x \in [-\pi, \pi] \quad (52)$$

478 in the second case. In order to apply our method, we first  
 479 produced finite simulation trajectories for both potentials. To  
 480 this end, we picked an (also artificial) time-step  $\Delta t = 10^{-3}$ , and  
 481 then used the Euler–Maruyama method, where position  $x_{k+1}$  is  
 482 computed from position  $x_k$  as

$$483 \quad x_{k+1} = x_k - \Delta t \nabla v(x_k) + \sqrt{2D\Delta t} y_t \quad (53)$$

$$484 \quad y_t \sim \mathcal{N}(0, 1) \quad (54)$$

485 In this way, we produced simulations of  $5 \times 10^6$  time-steps  
 486 for the harmonic potential and  $10^7$  time-steps for the double-  
 487 well potential.

488 **3.1.2. Gaussian Model.** We apply our method with Gaussian  
 489 basis functions to both problems. To this end,  $n = 2, 3, \dots, 10$   
 490 centers are chosen at uniform distance between  $x = -4$  and  $x =$   
 491  $4$  for the harmonic potential and between  $x = -\pi$  and  $x = \pi$  for  
 492 the double-well potential. In the latter case, the basis functions  
 493 are modified to be periodic on  $[-\pi, \pi]$ . Subsequently, an  
 494 “optimal” width of the Gaussians is picked by simply trying out  
 495 several choices for the standard deviations between 0.4 and 1.0  
 496 and using the one which yields the highest second eigenvalue.  
 497 From this choice, the matrices  $\mathbf{C}$  and  $\mathbf{S}$  are estimated and the  
 498 eigenvalues, functions, and implied time scales are computed.

499 **3.1.3. Markov Models.** As a reference for our methods, we  
 500 also compute Markov state models for both processes. To this  
 501 end, the simulation data is clustered into  $n = 2, 3, \dots, 10$  disjoint  
 502 clusters using the  $k$ -means algorithm. Subsequently, the EMMA  
 503 software package<sup>43</sup> is used to estimate the MSM transition  
 504 matrices and to compute eigenvalues and time scales.

505 **3.2. Alanine Dipeptide.** 3.2.1. *MD Simulations.* We  
 506 performed 20 simulations of 200 ns of all-atom explicit solvent  
 507 molecular dynamics of alanine dipeptide using the AMBER  
 508 ff-99SB-ILDN force field.<sup>71</sup> The detailed simulation setup is  
 509 found in Appendix E.

510 **3.2.2. Gaussian Model.** Similar to the previous example, we  
 511 use periodic Gaussian functions that only depend on one of the  
 512 two significant dihedral angles of the system (see section 4.2)  
 513 to apply our method. For both dihedrals, we separately perform  
 514 a preselection of the Gaussian trial functions. To this end, we  
 515 first project the data onto the coordinate, then we solve the  
 516 projected optimization problem for all possible choices of  
 517 centers and widths, and then pick the ones yielding the highest  
 518 eigenvalues. In every step of the optimization, we select three  
 519 out of four equidistributed centers between  $-\pi$  and  $\pi$ , and one

of eleven standard deviations between  $0.04\pi$  and  $0.4\pi$ . In this  
 way, we obtain three Gaussian trial functions per coordinate,  
 resulting in a full basis set of six functions. Having determined  
 the parameters for both angles, we use the resulting trial  
 functions to apply our method as before. A bootstrapping  
 procedure is used to estimate the statistical uncertainty of the  
 implied time scales.

Note that the variations of basis functions described here to  
 find a “good” basis set could be conducted once for each amino  
 acid (or short sequences of amino acids) for a given force field  
 and then be reused.

**3.2.3. Markov Models.** This time, we cluster the data into  
 $n = 5, 6, 10, 15, 20, 30, 50$  clusters, again using the  $k$ -means  
 algorithm. From these cluster-centers, we build Markov models  
 and estimate the eigenvalues and eigenvectors using the EMMA  
 software.

**3.3. Deca-alanine.** 3.3.1. *MD Simulations.* We performed  
 six 500 ns all-atom explicit solvent molecular-dynamics  
 simulations of deca-alanine using the Amber03 force field.  
 See Appendix E for the detailed simulation setup.

**3.3.2. Gaussian Model.** As before, we use Gaussian basis  
 functions that depend on the backbone dihedral angles of the  
 peptide, which means that we now have a total of 18 internal  
 coordinates. A preselection of the trial functions is performed  
 for every coordinate independently, similar to the alanine  
 dipeptide example. In order to keep the number of basis  
 functions acceptably small, we select two trial functions per  
 coordinate. As before, their centers are chosen from four  
 equidistributed centers along the coordinate, and their standard  
 deviations are chosen from eleven different values between  
 $0.04\pi$  and  $0.4\pi$ . We also build a second Gaussian model using  
 five functions per coordinate, with equidistributed centers and  
 standard deviations optimized from the same values as in the  
 first model. Having determined the trial functions, we estimate  
 the matrices  $\mathbf{C}$  and  $\mathbf{S}$  and compute the eigenvalues and  
 eigenvectors and again use bootstrapping to estimate  
 uncertainties.

**3.3.3. Markov Models.** We construct two different Markov  
 models from the dihedral angle data. The first is built using  
 $k$ -means clustering with 1000 cluster centers on the full data set,  
 whereas for the second, we divide the  $\phi$ – $\psi$  plane of every  
 dihedral pair along the chain into three regions corresponding  
 to the  $\alpha$ -helix,  $\beta$ -sheet, and left-handed  $\alpha$ -helix conformation,  
 see section 4.2. Thus, we have three discretization boxes for all  
 dihedral pairs, which yields a total of  $8^3$  discrete states to which  
 the trajectory points are assigned.

## 4. RESULTS

We now turn to the results obtained for the four systems  
 presented in the previous section.

**4.1. One-dimensional Potentials.** The two one-dimensional  
 systems are toy examples where all important properties are  
 either analytically known or can be computed arbitrarily well  
 from approximations. For the harmonic potential, the stationary  
 distribution is just a Gaussian function

$$|\pi(x)\rangle = |l_1(x)\rangle = \frac{1}{\sqrt{2\pi}} \exp\left(-\frac{x^2}{2}\right) \quad (55)$$

The exact eigenvalues  $\lambda_\alpha(\tau)$  are given by

$$\lambda_\alpha(\tau) = \exp(-(\alpha - 1)\tau) \quad (56)$$

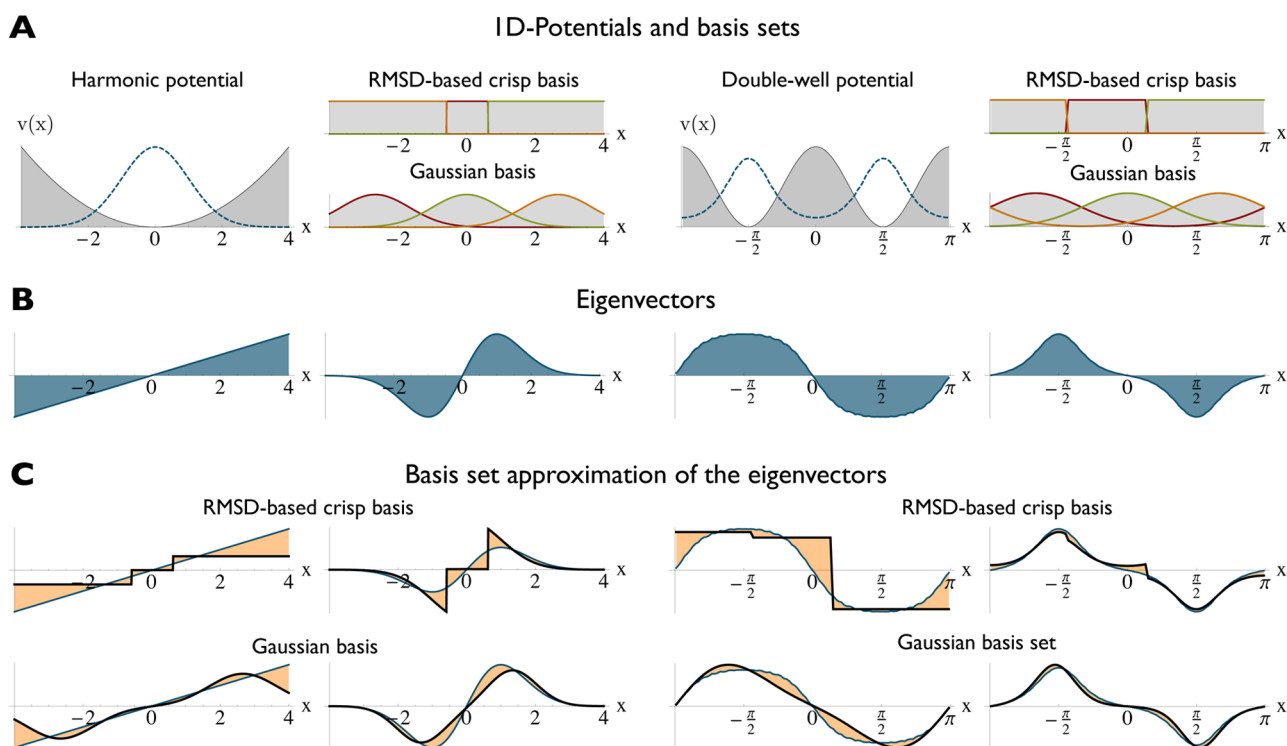


**Figure 2.** Illustration of the method with two one-dimensional potentials, the harmonic potential in the left half and a periodic double-well potential in the right half of the figure. (A) Potential  $v$  together with its invariant distribution  $\pi$  (shaded) next to two possible choices of basis functions: a three-element crisp basis and a set of three Gaussian functions. (B) Exact right and left second eigenfunctions,  $|r_2\rangle$  and  $|l_2\rangle$ . (C) Approximation results for these second eigenfunctions obtained from the basis sets shown.

576 and the associated right eigenfunction  $r_\alpha$  is given by the  
577  $(\alpha - 1)$ -th normalized Hermite polynomial

$$|r_\alpha(x)\rangle = |H_{\alpha-1}(x)\rangle \sim (-1)^{\alpha-1} \exp\left(\frac{x^2}{2}\right) \frac{d^{\alpha-1}}{dx^{\alpha-1}} \exp\left(-\frac{x^2}{2}\right) \quad (57)$$

578

579 The left halves of panels A and B in Figure 2 show the  
580 harmonic potential and its stationary distribution, as well as the  
581 second right and left eigenfunction. The sign change of  $|l_2\rangle$   
582 indicates the oscillation around the potential minimum, which  
583 is the slowest equilibration process. Note, however, that there is  
584 no energy barrier in the system; that is, this process is not  
585 metastable. On the right-hand sides of parts A and B in Figure 2,  
586 we see the same for the periodic double-well potential. The  
587 invariant density is equal to the Boltzmann distribution, where the  
588 normalization constant was computed numerically. The second  
589 eigenfunction was computed by a very fine finite-element  
590 approximation of the corresponding Fokker–Planck equation,  
591 using 1000 linear elements. The slowest transition in the system is  
592 the crossing of the barrier between the left and right minimum.  
593 This is reflected in the characteristic sign change of the second  
594 eigenfunction. Parts A and B of Figure 2 also show two choices of  
595 basis sets that can be used to approximate these eigenfunctions: A  
596 three element Gaussian basis set and a three state crisp set. The  
597 resulting estimates of the right and left eigenfunctions are  
598 displayed in Figure 2C. Already with these small basis sets, a  
599 good approximation is achieved.

600 Let us analyze the approximation quality of both methods  
601 in more detail. To this end, we first compute the  
602  $L^2$ -approximation error between the estimated second  
603 eigenfunction  $|\widehat{r}_2\rangle$  and the exact solution  $|r_2\rangle$ , that is, the  
604 integral

$$\delta = \int_X (|r_2\rangle(x) - |\widehat{r}_2\rangle(x))^2 \pi(x) dx \quad (58)$$

We expect this error to decay if the basis sets grow. Indeed, 605  
this is the case, as can be seen in the upper graphics of Figure 606  
3A and B, but the error produced by the Gaussian basis sets 607  
decays faster. Even for the 10-state MSM, we still have a 608  
significant approximation error. Another important indicator is 609  
the implied time scale  $t_\alpha(\tau)$ , associated to the eigenvalue  $\lambda_\alpha(\tau)$ . 610  
It is the inverse rate of exponential decay of the eigenvalue, 611  
given by  $t_\alpha(\tau) = -\tau/\lambda_\alpha(\tau)$  and corresponds to the equilibration 612  
time of the associated slow transition. The exact value of  $t_\alpha$  is 613  
independent of the lag time  $\tau$ . However, if we estimate the 614  
time scale from the approximate eigenvalues, the estimate 615  
will be too small due to the variational principle. However, 616  
with increasing lag time, the error is expected to decay, as 617  
the approximation error also decays with the lag time. The 618  
faster this decay occurs, the better the approximation will 619  
be. In the lower graphics of Figure 3A and B, we see the lag 620  
time dependence of the second time scale  $t_2$  for growing 621  
crisp and Gaussian basis sets. We observe that it takes only 622  
four to five Gaussian basis functions to achieve much faster 623  
convergence compared even to a 10-state Markov model. 624  
For seven or more Gaussian basis functions, we achieve 625  
precise estimates even for very short lag times, which cannot 626  
be achieved with Markov models with a reasonable number 627  
of states. 628

**4.2. Alanine Dipetide.** Alanine dipetide (Ac-Ala-NHMe, 629  
i.e. an alanine linked at either end to a protection group) is 630  
designed to mimic the dynamics of the amino acid alanine in a 631  
peptide chain. Unlike the previous examples, the eigenfunctions 632  
and eigenvalues of alanine dipetide cannot be calculated 633  
directly from its potential energy function but have to be 634



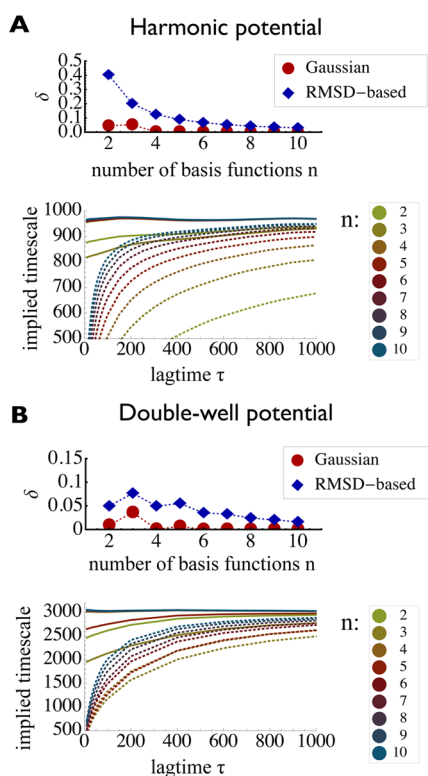


**Figure 3.** Analysis of the discretization error for both 1D-potentials. In the upper figure of both panels, we show the  $L^2$ -approximation error of the second eigenfunction from both crisp basis functions and Gaussian basis functions, dependent on the size of the basis set. The lower figures show the convergence of the second implied time scales  $t_2(\tau)$  dependent on the lag time  $\tau$ . Dotted lines represent the crisp basis sets and solid lines the Gaussian basis sets. The colors indicate the size of the basis.

635 estimated from simulations of its conformational dynamics.  
 636 However, alanine dipeptide is a thoroughly studied system;  
 637 many important properties are well-known, though their  
 638 estimated values depend on the precise potential energy  
 639 function (force field) used in the simulations. Most  
 640 importantly, it is known that the dynamical behavior can  
 641 essentially be understood in terms of the two backbone dihedral  
 642 angles  $\phi$  and  $\psi$ : Figure 4A shows the free energy landscape  
 643 obtained from population inversion of the simulation, where  
 644 white regions correspond to nonpopulated states. We find the  
 645 three characteristic minima in the upper left, central left, and  
 646 central right part of the plane, which correspond to the  $\beta$ -sheet,  
 647  $\alpha$ -helix, and left-handed  $\alpha$ -helix conformation of the amino  
 648 acid. The two slowest transitions occur between the left half  
 649 and the left handed  $\alpha$ -helix, and from  $\beta$ -sheet to  $\alpha$ -helix within  
 650 the main well on the left, respectively.

651 Figure 4B shows the weighted second and third eigenfunc-  
 652 tions. They are obtained from applying our method with a total  
 653 of six basis functions (three for each dihedral), and from an  
 654 MSM constructed from 30 cluster-centers. The resulting  
 655 estimates of  $|l_2\rangle$  and  $|l_3\rangle$  are then weighted with the population  
 656 estimated from the trajectory in order to emphasize the regions  
 657 of phase space which are related to the structural transitions.  
 658 Almost identical results are achieved, and the sign pattern of  
 659 both approximations clearly indicates the aforementioned  
 660 processes.

661 Lastly, in Figure 4C, we again investigate the convergence of  
 662 the slowest implied time scales. Different MSMs with a growing

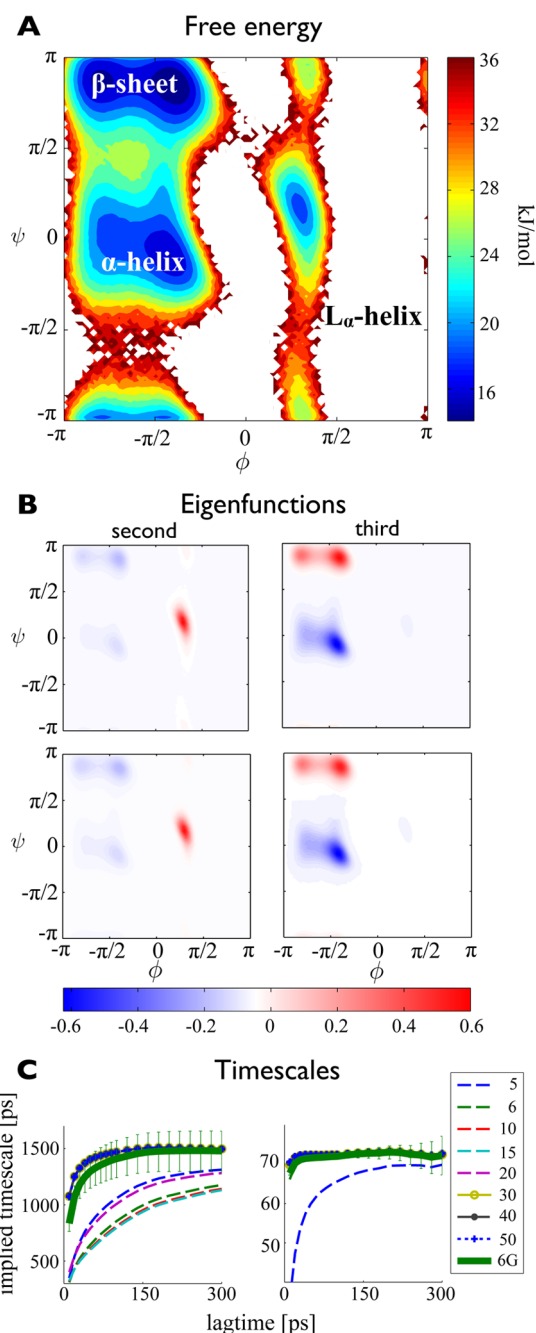


**Figure 4.** Illustration of the method using the 2D dihedral angle space  $(\phi, \psi)$  of alanine dipeptide trajectory data. (A) Free energy landscape obtained by direct population inversion of the trajectory data. (B1 and B2) Color-coded contour plots of the second and third eigenfunctions of the propagator  $(|l_2\rangle, |l_3\rangle)$ , obtained by approximating the functions  $|r_2\rangle$  and  $|r_3\rangle$  by a Gaussian basis set with six functions, cf eq 48, and weighting the results with the estimated stationary distribution from part A. (C1 and C2) Color-coded contour plots of the second and third eigenfunctions of the propagator  $(|l_2\rangle, |l_3\rangle)$ , obtained by approximating the functions  $|r_2\rangle$  and  $|r_3\rangle$  by a Markov state model with 30 cluster-centers, c.f. eq 48, and weighting the results with the estimated stationary distribution from part A. (D1 and D2) Convergence of implied time scales  $t_a(\tau)$  (in picoseconds) corresponding to the second and third eigenfunction, as obtained from Markov models using  $n = 5, 6, 10, 15, 20, 30, 50$  cluster-centers (thin lines), compared to the time scales obtained from the Gaussian model with a total of six basis functions (thick green line). Thin vertical bars indicate the error estimated by a bootstrapping procedure.



663 number of crisp basis functions (cluster-centers) were used and  
 664 compared to the six basis function Gaussian model. The colors  
 665 indicate the number of basis functions used; the thinner lines  
 666 correspond to the Markov models, whereas the thick solid line  
 667 is obtained from the Gaussian model. In agreement with the  
 668 previous results, we find that 30 or more crisp basis functions  
 669 are needed to reproduce an approximation quality similar to  
 670 that of a six-Gaussian basis set.

671 **4.3. Deca-alanine.** As a third and last example, we study  
 672 deca-alanine, a small peptide that is about five times the size  
 673 of alanine dipeptide. A sketch of the peptide is displayed in  
 674 Figure 5A.

675 The slow structural processes of deca-alanine are less obvious  
 676 compared to alanine dipeptide. The Amber03 force field used  
 677 in our simulation produces a relatively fast transition between

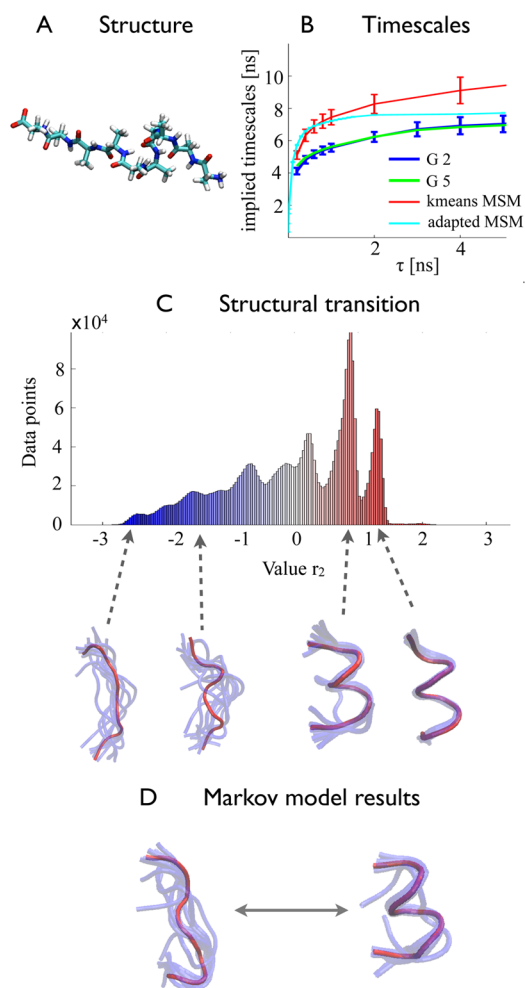


**Figure 5.** Illustration of the method using dihedral angle coordinates of the deca alanine molecule. (A) Graphical representation of the system. (B) Convergence of the estimated second implied time scale (in nanoseconds) depending on the lag time. We show the results of both Gaussian models and of both the kmeans based MSM and the adapted MSM. Thin vertical bars indicate the error estimated by a bootstrapping procedure. (C) Assignment of representative structures for the second slowest process: The histogram shows how the values of the second estimated eigenfunction  $|r_2\rangle$  of the smaller model are distributed over all simulation trajectories. Underneath, we show an overlay of structures taken at random from the vicinity of the peaks at  $-2.7$ ,  $-1.6$ ,  $0.7$ , and  $1.3$ . (D) Overlays of structures corresponding to the most negative (left) and most positive (right) values of the second Markov model eigenvector, taken from the *k*-means MSM.

the elongated and the helical state of the system, with an  
 associated time scale of 5–10 ns. As we can see in Figure 5B,  
 we are able to recover this slowest time scale with our method,  
 $t_2$  converges to roughly 6.5 ns for both models. Comparing this  
 to the two Markov models constructed from the same  
 simulation data, we see that both yield slightly higher time  
 scales: The *k*-means based MSM returns a value of about 8 ns  
 and the finely discretized one ends up with 8.5 ns. Note that the  
 underestimate of the present Gaussian basis set is systematic,  
 likely due to the fact that all basis functions were constructed as  
 a function of single dihedral angles only, thereby neglecting the  
 coupling between multiple dihedrals.

Despite this approximation, we are able to determine the  
 correct structural transition. In order to analyze this, we  
 evaluate the second eigenfunction  $|r_2\rangle$ , obtained from the  
 smaller model, for all trajectory points, and plot a histogram of  
 these values as displayed in Figure 5C. We then select all frames  
 that are within close distance of the peaks of that histogram and  
 produce overlays of these frames as shown underneath. Clearly,  
 large negative values of the second eigenfunction indicate that  
 the peptide is elongated, whereas large positive values indicate  
 that the helical conformation is attained. This is in accord  
 with a similar analysis of the second right Markov model  
 eigenvector: In Figure 5D, we show overlays of structures taken  
 from states with the most negative and most positive values of  
 the second eigenfunction, and we find that the same transition is  
 indicated, although the most negative values correspond to a  
 slightly more bent arrangement of the system.

In summary, it is possible to use a comparatively small basis  
 of 36 Gaussian functions to achieve results about the slowest  
 structural transition which are comparable to those of MSMs  
 constructed from about 1000 and 6500 discrete states,  
 respectively. However, the differences in the time scales point  
 to a weakness of the method: The fact that increasing the  
 number of basis functions does not alter the computed time  
 scale indicates that coordinate correlation cannot be appropri-  
 ately captured using sums of one-coordinate basis functions. In  
 order to use the method for larger systems, we will have to  
 study ways to overcome this problem.

## 5. CONCLUSIONS

We have presented a variational approach for computing the  
 slow kinetics of biomolecules. This approach is analogous to  
 the variational approach used for computing stationary states in  
 quantum mechanics, but it uses the molecular dynamics  
 propagator (or transfer operator) rather than the quantum-  
 mechanical Hamiltonian. A corresponding method of linear  
 variation is formulated. Since the MD propagator is not  
 analytically tractable for practically relevant cases, the matrix  
 elements cannot be directly computed. Fortunately, these  
 matrix elements can be shown to be correlation functions that  
 can be estimated from simple MD simulations. The method  
 proposed here is thus, to first define a basis set able to capture  
 the relevant conformational dynamics, then compute the  
 respective correlation matrices, and then to compute their  
 dominant eigenvalues and eigenvectors, thus obtaining the key  
 ingredients of the slow kinetics.

Markov state models (MSMs) are found to be a special case  
 of the variational principle formulated here, namely for the case  
 that indicator functions (also known as crisp sets or step  
 functions) on the MSM clusters are used as a basis set.

We have applied the variational approach using Gaussian  
 basis functions on a number of model examples, including

one-dimensional diffusion systems and simulations of the alanine dipeptide and deca-alanine in explicit solvent. Here, we have used only one-dimensional basis sets that were constructed on single coordinates (e.g., dihedral angles), but it is clear that multidimensional basis functions could be straightforwardly used. Despite the simplicity of our bases, we could recover, and in most cases improve the results of  $n$ -state MSMs with much less than  $n$  basis functions in the applications shown here.

Note that practically all MSM approaches presented thus far use data-driven approaches to find the clusters on which these indicator functions are defined. Such a data-driven approach impairs the comparability of Markov state models of different simulations of the same system, and even more so of Markov state models of different systems. (Essentially, every Markov state model that has been published so far has been parametrized with respect to its own unique basis set). In contrast, the method proposed here allows to define basis sets that are, in principle, transferable between different molecular systems. This improves the comparability of models made for different molecular systems. The second—and possibly decisive—advantage of the proposed method is that the basis sets can be chosen such that they reflect knowledge about the conformational dynamics or about the forcefield with which  $x_t$  has been simulated. It is thus conceivable that optimal basis sets are constructed for certain classes of small molecules or molecule fragments (e.g., amino acids or short amino acid sequences) and then combined for computing the kinetics of complex molecular systems.

As mentioned earlier, future work will have to focus on a systematic basis set selection and on an efficient use of multidimensional trial functions. Related to this is the question of model validation and error estimation. Due to the use of finite simulation data, use of a very fine basis set can lead to a growing statistical uncertainty of the estimated eigenvalues and eigenfunctions. In order to improve the basis set while balancing the model error and the statistical noise, a procedure to estimate this uncertainty is needed. While the special case of a Markov model allows for a solid error-theory based on the probabilistic interpretation of the model,<sup>72</sup> this is an open topic here and will have to be treated in the future.

## APPENDIX A

### Propagators of Reversible Processes

In the following, we explain in more detail the properties of the dynamical propagator  $\mathcal{P}(\tau)$ , as introduced in section 2.

**Stationary Density.** For any time-homogeneous propagator, there exists at least one stationary density  $|\pi(x)\rangle$ , which does not change under the action of the operator:  $\mathcal{P}(\tau)|\pi(x)\rangle = |\pi(x)\rangle$ . Another way of looking at this equation is to say that  $|\pi(x)\rangle$  is an eigenfunction of  $\mathcal{P}(\tau)$  with eigenvalue  $\lambda_1 = 1$ . It is guaranteed that  $\pi(x) \geq 0$  everywhere as the transfer density is normalized. We additionally assume that  $\pi(x) > 0$ . In molecular systems,  $\pi(x)$  is a Boltzmann density and  $\pi(x) > 0$  is obtained when the temperature is nonzero and the energy is finite for all molecular configurations.

**Bound Eigenvalue Spectrum.** The eigenvalue  $\lambda_1 = 1$  always exists for any propagator. It is also the eigenvalue with the largest absolute value  $|\lambda_i| \leq 1$ ; that is, the eigenvalue spectrum of  $\mathcal{P}(\tau)$  is bound from above by the value 1. This is due to the fact that the transfer density is normalized

$$\int_X p(x, y, \tau) dy = 1 \quad (59)$$

That is, the probability of going from state  $x_t = x$  to anywhere in the state space (including  $x$ ) during time  $\tau$  has to be 1.<sup>73,74</sup>

**Ergodicity.** If the dynamics of the molecule are ergodic, then  $\lambda_1$  is nondegenerate. As a consequence, there is only one unique stationary density  $\pi(x)$  associated to  $\mathcal{P}(\tau)$ .

**Reversibility.** If the dynamics of the individual molecules in the ensemble occur under equilibrium conditions, they fulfill reversibility (also sometimes called “detailed balance” or “micro-reversibility”) with respect to the stationary distribution  $\pi$

$$\pi(x)p(x, y; \tau) = \pi(y)p(y, x; \tau) \quad \forall x, y \quad (60)$$

Equation 60 implies that if the ensemble is in equilibrium, that is, its systems are distributed over the state space according to  $|\pi(x)\rangle$ , the number of systems going from state  $x$  to state  $y$  during time  $\tau$  is the same as the number of systems going from  $y$  to  $x$ . Or, the density flux from  $x$  to  $y$  is the same as in the opposite direction, and this is true for all state pairs  $\{x, y\}$ . For reversible processes, the stationary density becomes an equilibrium density and is equal to the Boltzmann distribution. In the following, we will only consider operators of reversible processes.

A consequence of reversibility is that  $\lambda_1$  is the only eigenvalue with absolute value 1. Together with the previous properties, the eigenvalues can be sorted by their absolute value

$$|\lambda_1| = 1 > |\lambda_2| \geq |\lambda_3| \dots \quad (61)$$

**Self-adjoint Operator.** Another consequence of reversibility is self-adjointness of the propagator, that is,

$$\langle f | \mathcal{P}(\tau) | g \rangle_{\pi^{-1}} = \langle g | \mathcal{P}(\tau) | f \rangle_{\pi^{-1}} \quad (62)$$

with respect to the weighted scalar product  $\langle \cdot | \cdot \rangle_{\pi^{-1}}$

$$\langle f | g \rangle_{\pi^{-1}} = \int_X \overline{g(x)} \pi^{-1}(x) f(x) dx \quad (63)$$

and the norm

$$|f| = \sqrt{\langle f | f \rangle_{\pi^{-1}}} \quad (64)$$

where  $\pi^{-1}(x) = 1/\pi(x)$  is the reciprocal function of  $\pi(x)$  and the bar denotes complex conjugation. This is verified directly:

$$\langle \mathcal{P}(\tau) f | g \rangle_{\pi^{-1}} = \int_X \left[ \int_X p(x, y, \tau) f(x) dx \right] \pi^{-1}(y) g(y) dy \quad (65)$$

$$= \int_X \left[ \int_X p(y, x, \tau) \frac{\pi(y)}{\pi(x)} f(x) dx \right] \pi^{-1}(y) g(y) dy \quad (66)$$

$$= \int_X \int_X p(y, x, t) f(x) \pi^{-1}(x) g(y) dy dx \quad (67)$$

$$= \int_X f(x) p^{-1}(x) \left[ \int_X p(y, x, t) g(y) dy \right] dx \quad (68)$$

$$= f | \mathcal{P}(\tau) g \rangle_{\pi^{-1}} \quad (69)$$

In the second line, we have used reversibility (eq 60) to replace  $p(x, y, \tau)$  by  $p(y, x, \tau) \pi(y) / \pi(x)$ . Note that we could omit the complex conjugate in eq 63 because  $f$ ,  $\mathcal{P}(\tau)$ , and  $g$  are real-valued functions. Self-adjointness of  $\mathcal{P}(\tau)$  implies that its eigenvalues are real-valued, and its eigenfunctions form a complete basis of

$\mathbb{R}^{3N}$  which is orthonormal with respect to the weighted scalar product  $\langle \cdot | \cdot \rangle_{\pi^{-1}}$

$$\langle I_\alpha | I_\beta \rangle_{\pi^{-1}} = \delta_{\alpha\beta} \quad (70)$$

**Comparison to the QM Hamilton Operator.** With these properties of the propagator, eq 6 can be compared to the

stationary Schrödinger equation  $\mathcal{H}|\chi\rangle = E|\chi\rangle$ . Both equations are eigenvalue equations of self-adjoint operators with a bound eigenvalue spectrum. The equations differ in some mathematical aspects:  $\mathcal{P}(\tau)$  is an integral operator, whereas  $\mathcal{H}$  is a differential operator;  $\mathcal{P}(\tau)$  is self-adjoint with respect to a weighted scalar product, whereas  $\mathcal{H}$  is self-adjoint with respect to the Euclidean scalar product. Also, they are not analogous in their physical interpretation. In contrast to the quantum-mechanical Hamilton operator, which acts on complex-valued wave functions,  $\mathcal{P}(\tau)$  propagates real-valued probability densities. Moreover, the eigenfunctions of the propagator do not represent quantum states, such as the ground and excited states, they represent the stationary distribution and the perturbations to the stationary distribution from kinetic processes. Nonetheless, the mathematical structures of eq 6 and the stationary Schrödinger equation are similar enough that some methods which are applied in quantum chemistry can be reformulated for the propagator.

## APPENDIX B

### Variational Principle

The variational principle for propagators is derived and discussed in detail in ref 65. We expand a trial function in terms of the eigenfunctions of  $\mathcal{P}(\tau)$

$$|f\rangle = \sum_{\alpha} c_{\alpha} |l_{\alpha}\rangle \quad (71)$$

where the  $\alpha$ th expansion coefficients is given as

$$c_{\alpha} = \langle l_{\alpha} | f \rangle_{\pi^{-1}} \quad (72)$$

The norm (eq 64) of the trial function  $|f\rangle$  is then given as

$$\langle f | f \rangle_{\pi^{-1}} = \sum_{\alpha} \sum_{\beta} c_{\alpha} c_{\beta} \langle l_{\alpha} | l_{\beta} \rangle_{\pi^{-1}} = \sum_{\alpha} c_{\alpha}^2 \quad (73)$$

We therefore require that  $|f\rangle$  is normalized

$$\langle f | f \rangle_{\pi^{-1}} = 1 \quad (74)$$

With this, an upper bound for the following expression can be found

$$\langle f | \mathcal{P}(\tau) | f \rangle_{\pi^{-1}} = \sum_{\alpha} \sum_{\beta} c_{\alpha} c_{\beta} \langle l_{\alpha} | \mathcal{P}(\tau) | l_{\beta} \rangle_{\pi^{-1}} \quad (75)$$

$$= \sum_{\alpha} \sum_{\beta} c_{\alpha} c_{\beta} \lambda_{\beta} \langle l_{\alpha} | l_{\beta} \rangle_{\pi^{-1}} \quad (76)$$

$$= \sum_{\alpha} c_{\alpha}^2 \lambda_{\alpha} \quad (77)$$

$$\leq \sum_{\alpha} c_{\alpha}^2 \lambda_1 = \langle f | f \rangle_{\pi^{-1}} \lambda_1 = 1 \quad (78)$$

and hence

$$\lambda_1 = 1 \geq \langle f | \mathcal{P}(\tau) | f \rangle_{\pi^{-1}} \quad (79)$$

The above functional of any trial function is smaller than or equal to one, where the equality only holds if and only if  $|f\rangle = |l_1\rangle$ .

Furthermore, from the equations above it directly follows that for a function  $f_i$  that is orthogonal to eigenfunctions  $|l_1\rangle, \dots, |l_{i-1}\rangle$ :

$$\langle f_i | l_j \rangle_{\pi^{-1}} = 0 \quad \forall j = 1, \dots, i-1 \quad (80)$$

the variational principle results in

$$\langle f | \mathcal{P}(\tau) | f \rangle_{\pi^{-1}} \leq \lambda_i \quad (81)$$

## APPENDIX C

### Method of Linear Variation

Given the variational principle for the transfer operator (eq 79), the function  $|f\rangle$  can be linearly expanded using a basis of  $n$  basis functions  $\{|\varphi_i\rangle\}_{i=1}^n$

$$f = \sum_{i=1}^n a_i |\varphi_i\rangle \quad (82)$$

where  $a_i$  are the expansion coefficients. All basis functions are real functions, but the basis set is not necessarily orthonormal. Hence, the expansion coefficients are real numbers. In the method of linear variation, the expansion coefficients  $a_i$  are varied such that the right-hand side of eq 79 becomes maximal, while the basis functions are kept constant. The derivation leads to matrix formulation of eq 6. Solving the corresponding matrix diagonalization problem, one obtains the first  $n$  eigenvectors of  $\mathcal{P}(\tau)$  expressed in the basis  $\{|\varphi_i\rangle\}_{i=1}^n$  and the associated eigenvalues. Inserting eq 16 into eq 79 obtains

$$1 \geq \left\langle \sum_{i=1}^n a_i \varphi_i | \mathcal{P} | \sum_{j=1}^n a_j \varphi_j \right\rangle_{\pi^{-1}} \quad (83)$$

$$= \sum_{i,j=1}^n a_i a_j \langle \varphi_i | \mathcal{P} | \varphi_j \rangle_{\pi^{-1}} \quad (84)$$

$$= \sum_{i,j=1}^n a_i a_j \langle \varphi_i | \mathcal{P} | \varphi_j \rangle_{\pi^{-1}} \quad (85)$$

where we have introduced the matrix element of the correlation matrix **C**

$$C_{ij} = \langle \varphi_i | \mathcal{P} | \varphi_j \rangle_{\pi^{-1}} \quad (86)$$

The maximum of the expression of right-hand side in eq 79 is found by varying the coefficients  $a_i$ , that is,

$$\frac{\partial}{\partial a_k} \langle f | \mathcal{P} | f \rangle_{\pi^{-1}} = \frac{\partial}{\partial a_k} \sum_{ij=1}^n a_i a_j C_{ij} \quad (87)$$

$$= 0 \quad \forall k = 1, 2, \dots, n \quad (88)$$

under the constraint that  $|f\rangle$  is normalized

$$\langle f | f \rangle_{\pi^{-1}} = \sum_{ij=1}^n a_i a_j \langle \varphi_i | \varphi_j \rangle_{\pi^{-1}} = \sum_{ij=1}^n a_i a_j S_{ij} \quad (89)$$

$$= 1 \quad (90)$$

$S_{ij}$  is the matrix element of the overlap matrix **S** defined as

$$S_{ij} = \langle \varphi_i | \varphi_j \rangle_{\pi^{-1}} = \langle \varphi_j | \varphi_i \rangle_{\pi^{-1}} \quad (91)$$

To incorporate the constraint in the optimization problem, we make use of the method of Lagrange multipliers



$$\mathcal{L} = \sum_{ij=1}^n a_i a_j \langle \varphi_i | \mathcal{P} | \varphi_j \rangle_{\pi^{-1}} \quad (92)$$

$$- \lambda \left[ \sum_{ij=1}^n a_i a_j \langle \varphi_i | \varphi_j \rangle_{\pi^{-1}} - 1 \right] \quad (93)$$

$$= \sum_{ij=1}^n a_i a_j C_{ij} - \lambda \left[ \sum_{ij=1}^n a_i a_j S_{ij} - 1 \right] \quad (94)$$

910 The variational problem then is

$$\frac{1}{2} \frac{\partial}{\partial a_k} \mathcal{L} = \frac{1}{2} \sum_{j=1}^n a_j C_{ij} + \frac{1}{2} \sum_{i=1}^n a_i C_{ij} \quad (95)$$

$$- \frac{1}{2} \lambda \left[ \sum_{j=1}^n a_j S_{ij} + \sum_{i=1}^n a_i S_{ij} \right] \quad (96)$$

$$= \sum_{i=1}^n a_i C_{ij} - \lambda \sum_{i=1}^n a_i S_{ij} \quad (97)$$

$$= 0 \quad (98)$$

$$\forall k = 1, 2, \dots, n \quad (99)$$

911 where, in the third line, we have used that  $C_{ij} = C_{ji}$  and  $S_{ij} = S_{ji}$   
912 (eqs 62 and 91). Equation 95 can be rewritten as a matrix  
913 equation

$$914 \quad \mathbf{Ca} = \lambda \mathbf{Sa} \quad (100)$$

915 which is a generalized eigenvalue problem, and identical to

$$916 \quad \mathbf{S}^{-1} \mathbf{Ca} = \lambda \mathbf{a} \quad (101)$$

917 where  $\mathbf{a}$  is a vector which contains the coefficients  $a_i$ . The  
918 solutions of eq 101 are orthonormal with respect to an inner  
919 product which is weighted by the overlap matrix  $\mathbf{S}$ :

$$920 \quad \langle \mathbf{a}^f | \mathbf{S} | \mathbf{a}^g \rangle = \delta_{fg} \quad (102)$$

921 where  $\delta_{fg}$  is the Kronecker delta. Then, any two functions  $f =$   
922  $\sum_i a_i^f | \varphi_i \rangle$  and  $g = \sum_i a_i^g | \varphi_i \rangle$  are orthonormal with respect to the  
923  $\pi^{-1}$ -weighted inner product, as it is expected for the  
924 eigenfunctions of the transfer operator

$$\langle f | g \rangle_{\pi^{-1}} = \left\langle \sum_i a_i^f \varphi_i \left| \sum_j a_j^g \varphi_j \right. \right\rangle_{\pi^{-1}} \quad (103)$$

$$= \langle \mathbf{a}^f | \mathbf{S} | \mathbf{a}^g \rangle \quad (104)$$

$$= \delta_{fg} \quad (105)$$

## 925 ■ APPENDIX D

### 926 Left Eigenvectors and Stationary Properties

927 We want to show that the first “left” eigenvector  $\mathbf{b}_1 = \mathbf{S} \mathbf{a}_1$   
928 approximates the stationary distribution even for basis sets  
929 that do not form a partition of unity.

930 Let us assume we have a sequence of basis sets  $\{\chi_i\}_j$  such  
931 that the corresponding first eigenvalue  $\lambda_{1j}$  converges to 1. Let us  
932 denote the local densities of basis set  $j$  by  $Z_j^i$ , the total density  
933 from eq 47 by  $C^j$ , and the entries of the normalized first left  
934 eigenvector of basis set  $j$  by  $b_i^j$ . We show

$$935 \quad b_i^j - \frac{Z_i^j}{C^j} \rightarrow 0 \quad (106)$$

as  $j \rightarrow \infty$ , or in other words,

$$b_i^j C^j - Z_i^j \rightarrow 0 \quad (107) \quad 937$$

To do so, we multiply by the inverse partition function  $1/Z$   
938 and rewrite this expression as

$$\frac{1}{Z} (b_i^j C^j - Z_i^j) = \frac{1}{Z} \frac{\sum_k a_k^j s_{ik}^j}{(\sum_{l,k} a_k^j s_{lk}^j)} \int \sum_l \chi_{lj} e^{-v(x)} - \frac{1}{Z} \int \chi_{ij} e^{-v(x)} \quad (108)$$

$$= \frac{\sum_k a_k^j \chi_{kj} | \chi_{kj} \rangle_{\pi}}{\sum_{l,k} a_k^j \chi_{lj} | \chi_{lj} \rangle_{\pi}} \langle \sum_l \chi_{lj} | 1 \rangle_{\pi} - \langle \chi_{ij} | 1 \rangle_{\pi} \quad (109)$$

We can use eq 48 to pull the summation over  $k$  into the second  
940 argument of the brackets:

$$\frac{1}{Z} (b_i^j C^j - Z_i^j) = \frac{\langle \chi_{ij} | r_{1j} \rangle_{\pi}}{\langle \sum_l \chi_{lj} | 1 \rangle_{\pi}} \langle \sum_l \chi_{lj} | 1 \rangle_{\pi} - \langle \chi_{ij} | 1 \rangle_{\pi} \quad (110) \quad 942$$

From the convergence of the eigenvalue  $\lambda_{1j}$  toward 1, it  
943 follows that the approximate first eigenfunction  $| r_{1j} \rangle_{\pi}$  converges  
944 to the true first eigenfunction, the constant function with value  
945 one, in the space  $L^2_{\pi}$ . This can be shown using an orthonormal  
946 basis expansion. Consequently, we can use the Cauchy–  
947 Schwarz inequality to estimate the expression

$$|\langle \chi_{ij} | r_{1j} \rangle_{\pi} - \langle \chi_{ij} | 1 \rangle_{\pi}| = |\langle \chi_{ij} | r_{1j} - 1 \rangle_{\pi}| \quad (111) \quad 949$$

$$\leq \| \chi_{ij} \| \| r_{1j} - 1 \| \quad (112) \quad 950$$

As the second term tends to zero by the  $L^2$ -convergence, the  
951 complete expression likewise decays to zero, provided that the  
952  $L^2$ -norms of the basis functions remain bounded, which is  
953 reasonable to assume. By a similar argument, we can show that  
954 the remaining fraction  
955

$$\frac{\langle \sum_l \chi_{lj} | 1 \rangle_{\pi}}{\langle \sum_l \chi_{lj} | r_{1j} \rangle_{\pi}} \quad (113) \quad 956$$

converges to 1, provided that the  $L^2$ -norm of the sum of all  
957 basis functions also remains bounded. Combining these two  
958 observations, we can conclude that eq 110 tends to 0, which  
959 was to be shown. 960

## 961 ■ APPENDIX E

### Simulation Setups

962 *Alanine dipeptide.* We performed all-atom molecular  
963 dynamics simulations of acetyl-alanine-methylamide (Ac-Ala-  
964 NHMe), referred to as alanine dipeptide in the text, in explicit  
965 water using the GROMACS 4.5.5<sup>75</sup> simulation package, the  
966 AMBER ff-99SB-ILDN force field,<sup>71</sup> and the TIP3P water  
967 model.<sup>76</sup> The simulations were performed in the canonical  
968 ensemble at a temperature of 300 K. The energy-minimized  
969 starting structure of Ac-Ala-NHMe was solvated into a cubic  
970 box with a minimum distance between solvent and box wall of  
971 1 nm, corresponding to a box volume of 2.72 nm<sup>3</sup> and 651 water  
972 molecules. After an initial equilibration of 100 ps, 20 production  
973 runs of 200 ns each were performed, yielding a total simulation  
974 time of 4  $\mu$ s. Covalent bonds to hydrogen atoms were constrained  
975 using the LINCS algorithm<sup>77</sup> (lincs\_iter = 1, lincs\_order = 4),  
976 allowing for an integration time step of 2 fs. The leapfrog  
977 integrator was used. The temperature was maintained by the  
978 velocity-rescale thermostat<sup>78</sup> with a time constant of 0.01 ps.  
979 Lennard-Jones interactions were cut off at 1 nm. Electrostatic  
980 interactions were treated by the Particle–Mesh Ewald (PME)  
981

algorithm<sup>79</sup> with a real space cutoff of 1 nm, a grid spacing of 0.15 nm, and an interpolation order of 4. Periodic boundary conditions were applied in the *x*-, *y*-, and *z*-direction. The trajectory data was stored every 1 ps.

**Deca-alanine.** We performed all-atom molecular dynamics simulations of deca alanine, which is protonated at the amino terminus and deprotonated at the carboxy terminus, using the GROMACS 4.5.5 simulation package,<sup>75</sup> the Amber03 force field, and the TIP3P water model. A completely elongated conformation was chosen as an initial structure.

The structure was solvated in a cubic box of volume  $V = 232.6 \text{ nm}^3$ , with 7647 pre-equilibrated TIP3P water molecules. First, an equilibration run of 500 ps in the NVT ensemble with full position restraints, using the velocity-rescale thermostat, was carried out. This was followed by a 500 ps NPT equilibration run. The temperature was set to  $T = 300 \text{ K}$ . The equilibration run was followed by a 500 ns production run, again at  $T = 300 \text{ K}$ . Two temperature coupling groups were used with a velocity-rescale thermostat and a time constant of 0.01 ps.<sup>78</sup> Periodic boundary conditions were applied in the *x*-, *y*-, and *z*-direction. For the long-range electrostatic interaction PME was used with a pme-order of 4 and a Fourier grid spacing of 0.15 nm. Covalent bonds to hydrogen bonds were constrained using the LINCS algorithm,<sup>77</sup> allowing for a 2 fs time step. A leapfrog integrator was used. Data was saved every 1 ps, resulting in  $5 \times 10^5$  data frames. Six independent simulations from the same equilibrated configuration were carried out resulting in 3  $\mu\text{s}$  total data.

## AUTHOR INFORMATION

### Corresponding Authors

\*E-mail: bettina.keller@fu-berlin.de.

\*E-mail: frank.noe@fu-berlin.de.

### Notes

The authors declare no competing financial interest.

## ACKNOWLEDGMENTS

The authors thank Francesca Vitalini for providing the molecular dynamics simulation of alanine dipeptide.

## REFERENCES

- (1) Alberts, B.; Johnson, A.; Lewis, J.; Raff, M.; Roberts, K.; Walter, P. *Mol. Biol. Cell*, 5th ed.; Garland Science: New York, 2008.
- (2) Elber, R. *Simulations of allosteric transitions*. 2011; <http://www.ncbi.nlm.nih.gov/pubmed/21333527> (accessed Jan. 9, 2014).
- (3) Verhey, K. J.; Kaul, N.; Soppina, V. *Annu. Rev. Biophys.* **2011**, *40*, 267–288.
- (4) Dunkle, J. a.; Cate, J. H. D. *Annu. Rev. Biophys.* **2010**, *39*, 227–244.
- (5) Keller, B.; Daura, X.; Van Gunsteren, W. F. *J. Chem. Phys.* **2010**, *132*, 074110.
- (6) Krivov, S. V.; Karplus, M. *Proc. Natl. Acad. Sci. U.S.A.* **2004**, *101*, 14766–14770.
- (7) Wales, D. J. *Energy Landscapes*, 1st ed.; Cambridge University Press: Cambridge, 2003.
- (8) Noé, F.; Fischer, S. *Curr. Opin. Struc. Biol.* **2008**, *18*, 154–162.
- (9) Karpen, M. E.; Tobias, D. J.; Brooks, C. L. *Biochemistry* **1993**, *32*, 412–420.
- (10) Hubner, I. A.; Deeds, E. J.; Shakhnovich, E. I. *Proc. Natl. Acad. Sci. U.S.A.* **2006**, *103*, 17747–17752.
- (11) Buchete, N.; Hummer, G. *J. Phys. Chem. B* **2008**, *112*, 6057–6069.
- (12) Rao, F.; Cafisch, A. *J. Mol. Biol.* **2004**, *342*, 299–306.
- (13) Muff, S.; Cafisch, A. *Proteins* **2007**, *70*, 1185–1195.

- (14) de Groot, B.; Daura, X.; Mark, A.; Grubmüller, H. *J. Mol. Biol.* **2001**, *301*, 299–313.
- (15) Schultheis, V.; Hirschberger, T.; Carstens, H.; Tavan, P. *J. Chem. Theory Comp.* **2005**, *1*, 515–526.
- (16) Pan, A. C.; Roux, B. *J. Chem. Phys.* **2008**, *129*, 064107.
- (17) Weber, M. *Improved Perron Cluster Analysis*, Technical Report 03-04; Konrad-Zuse-Zentrum für Informationstechnik Berlin: Berlin-Dahlem, Germany, 2003.
- (18) Noé, F.; Krachtus, D.; Smith, J. C.; Fischer, S. *J. Chem. Theory Comput.* **2006**, *2*, 840–857.
- (19) Noé, F.; Oswald, M.; Reinelt, G.; Fischer, S.; Smith, J. C. *Multiscale Model. Simul.* **2006**, *5*, 393–419.
- (20) Noé, F.; Horenko, I.; Schütte, C.; Smith, J. C. *J. Chem. Phys.* **2007**, *126*, 155102.
- (21) Chodera, J. D.; Dill, K. A.; Singhal, N.; Pande, V. S.; Swope, W. C.; Pitera, J. W. *J. Chem. Phys.* **2007**, *126*, 155101.
- (22) Swope, W. C.; Pitera, J. W.; Suits, F. *J. Phys. Chem. B* **2004**, *108*, 6571–6581.
- (23) Swope, W. C.; Pitera, J. W.; Suits, F. *J. Phys. Chem. B* **2004**, *108*, 6571–6581.
- (24) Buchete, N.-V.; Hummer, G. *J. Phys. Chem. B* **2008**, *112*, 6057–6069.
- (25) Prinz, J.-H.; Wu, H.; Sarich, M.; Keller, B.; Senne, M.; Held, M.; Chodera, J. D.; Schütte, C.; Noé, F. *J. Chem. Phys.* **2011**, *134*, 174105.
- (26) E, W.; Vanden-Eijnden, E. *J. Stat. Phys.* **2006**, *123*, 503–523.
- (27) Noé, F.; Schütte, C.; Vanden-Eijnden, E.; Reich, L.; Weikl, T. R. *Proc. Natl. Acad. Sci. U.S.A.* **2009**, *106*, 19011–6.
- (28) Deuffhard, P.; Weber, M. *Linear Algebra and Its Applications* **2005**, *398*, 161–184.
- (29) Kube, S.; Weber, M. *J. Chem. Phys.* **2007**, *126*, 024103.
- (30) Chodera, J. D.; Singhal, N.; Pande, V. S.; Dill, K.; Swope, W. C. *J. Chem. Phys.* **2007**, *126*, 155101.
- (31) Noé, F.; Horenko, I.; Schütte, C.; Smith, J. C. *J. Chem. Phys.* **2007**, *126*, 155102.
- (32) Ruzhytska, S.; Jacobi, M. N.; Jensen, C. H.; Nerukh, D. *J. Chem. Phys.* **2010**, *133*, 164102.
- (33) Bowman, G. R.; Pande, V. S. *Proc. Natl. Acad. Sci. U.S.A.* **2010**, *107*, 10890–10895.
- (34) Noé, F.; Doose, S.; Daidone, I.; Löllmann, M.; Sauer, M.; Chodera, J. D.; Smith, J. C. *Proc. Natl. Acad. Sci. U.S.A.* **2011**, *108*, 4822–4827.
- (35) Keller, B. G.; Prinz, J.-H.; Noé, F. *Chem. Phys.* **2012**, *396*, 92–107.
- (36) Keller, B.; Hünenberger, P.; van Gunsteren, W. F. *J. Chem. Theory Comput.* **2011**, *7*, 1032–1044.
- (37) Singhal, N.; Pande, V. S. *J. Chem. Phys.* **2005**, *123*, 204909.
- (38) Noé, F. *J. Chem. Phys.* **2008**, *128*, 244103.
- (39) Chodera, J. D.; Noé, F. *J. Chem. Phys.* **2010**, *133*, 105102.
- (40) Bowman, G. R.; Beauchamp, K. A.; Boxer, G.; Pande, V. S. *J. Chem. Phys.* **2009**, *131*, 124101.
- (41) Pande, V. S.; Beauchamp, K.; Bowman, G. R. *Methods* **2010**, *52*, 99–105.
- (42) Beauchamp, K. A.; Bowman, G. R.; Lane, T. J.; Maibaum, L.; Haque, I. S.; Pande, V. S. *J. Chem. Theory Comput.* **2011**, *7*, 3412–3419.
- (43) Senne, M.; Trendelkamp-Schroer, B.; Mey, A. S. J. S.; Schütte, C.; Noé, F. *J. Chem. Theory Comput.* **2012**, *8*, 2223–2238.
- (44) Muff, S.; Cafisch, A. *Proteins: Struct. Funct. Bioinf.* **2007**, *70*, 1185–1195.
- (45) Lane, T. J.; Bowman, G. R.; Beauchamp, K.; Voelz, V. a.; Pande, V. S. *J. Am. Chem. Soc.* **2011**, *133*, 18413–18419.
- (46) Noé, F.; Schütte, C.; Vanden-Eijnden, E.; Reich, L.; Weikl, T. *Proc. Natl. Acad. Sci. U.S.A.* **2009**, *106*, 19011–19016.
- (47) Beauchamp, K. A.; McGibbon, R.; Lin, Y.-S.; Pande, V. S. *Proc. Natl. Acad. Sci. U.S.A.* **2012**, *109*, 17807–17813.
- (48) Shaw, D. E.; Maragakis, P.; Lindorff-Larsen, K.; Piana, S.; Dror, R. O.; Eastwood, M. P.; Bank, J. A.; Jumper, J. M.; Salmon, J. K.; Shan, Y.; Wrighers, W. *Science* **2010**, *330*, 341–346.

- 1111 (49) Lindorff-Larsen, K.; Piana, S.; Dror, R. O.; Shaw, D. E. *Science*  
1112 **2011**, 334, 517–520.
- 1113 (50) Sadiq, S. K.; Noé, F.; De Fabritiis, G. *Proc. Natl. Acad. Sci. U.S.A.*  
1114 **2012**, 109, 20449–20454.
- 1115 (51) Buch, L.; Giorgino, T.; De Fabritiis, G. *Proc. Natl. Acad. Sci.*  
1116 *U.S.A.* **2011**, 108, 10184–10189.
- 1117 (52) Kelley, N. W.; Vishal, V.; Krafft, G. A.; Pande, V. S. *J. Chem.*  
1118 *Phys.* **2008**, 129, 214707.
- 1119 (53) Nerukh, D.; Jensen, C. H.; Glen, R. C. *J. Chem. Phys.* **2010**, 132,  
1120 084104.
- 1121 (54) Jensen, C. H.; Nerukh, D.; Glen, R. C. *J. Chem. Phys.* **2008**, 128,  
1122 115107.
- 1123 (55) Sarich, M.; Noé, F.; Schütte, C. *Multiscale Model. Simul.* **2010**, 8,  
1124 1154–1177.
- 1125 (56) Altis, A.; Nguyen, P. H.; Hegger, R.; Stock, G. *J. Chem. Phys.*  
1126 **2007**, 126, 244111.
- 1127 (57) Schwantes, C.; Pande, V. *J. Chem. Theory Comput.* **2013**, 9,  
1128 2000–2009.
- 1129 (58) Pérez-Hernández, G.; Paul, F.; Giorgino, T.; De Fabritiis, G.;  
1130 Noé, F. *J. Chem. Phys.* **2013**, 139, 015102.
- 1131 (59) Schütte, C.; Fischer, A.; Huisinga, W.; Deuffhard, P. *J. Comput.*  
1132 *Phys.* **1999**, 151, 146–168.
- 1133 (60) Rains, E. K.; Andersen, H. C. *J. Chem. Phys.* **2010**, 133, 144113.
- 1134 (61) Weber, M. Ph.D. thesis, Freie Universitaet Berlin, Berlin, 2006.
- 1135 (62) Röblitz, S. Ph.D. thesis, Freie Universitaet Berlin, Berlin, 2009.
- 1136 (63) Haack, F.; Röblitz, S.; Scharkoi, O.; Schmidt, B. *AIP Conf. Proc.*  
1137 **2010**, 1281, 1585–1588.
- 1138 (64) Schütte, C.; Noé, F.; Lu, J.; Sarich, M.; Vanden-Eijnden, E. *J.*  
1139 *Chem. Phys.* **2011**, 134, 204105.
- 1140 (65) Noé, F.; Nüske, F. *SIAM Multiscale Model. Simul.* **2013**, 11,  
1141 635–655.
- 1142 (66) Szabo, A.; Ostlund, N. S. *Modern Quantum Chemistry*, 1st ed.;  
1143 Dover Publications: Mineola, NY, 1996; pp 31–38.
- 1144 (67) Noé, F.; Doose, S.; Daidone, I.; Löllmann, M.; Chodera, J.;  
1145 Sauer, M.; Smith, J. *Proc. Natl. Acad. Sci. U.S.A.* **2011**, 108, 4822–4827.
- 1146 (68) Lindner, B.; Yi, Z.; Prinz, J.-H.; Smith, J.; Noé, F. *J. Chem. Phys.*  
1147 **2013**, 139, 175101.
- 1148 (69) Zheng, Y.; Lindner, B.; Prinz, J.-H.; Noé, F.; Smith, J. *J. Chem.*  
1149 *Phys.* **2013**, 139, 175102.
- 1150 (70) Vanden-Eijnden, E.; Venturoli, M. *J. Chem. Phys.* **2009**, 130,  
1151 194101.
- 1152 (71) Lindorff-Larsen, K.; Piana, S.; Palmo, K.; Maragakis, P.; Klepeis,  
1153 J. L.; Dror, R. O.; Shaw, D. E. *Proteins* **2010**, 78, 1950–1958.
- 1154 (72) Prinz, J.-H.; Wu, H.; Sarich, M.; Keller, B.; Senne, M.; Held, M.;  
1155 Chodera, J.; Schütte, C.; Noé, F. *J. Chem. Phys.* **2011**, 134, 174105.
- 1156 (73) Deuffhard, P.; Huisinga, W.; Fischer, A.; Schütte, C. *Linear*  
1157 *Algebra and Its Applications* **2000**, 315, 39–59.
- 1158 (74) MacCluer, C. R. *SIAM Rev.* **2000**, 42, 487–498.
- 1159 (75) Van Der Spoel, D.; Lindahl, E.; Hess, B.; Groenhof, G.; Mark, A.  
1160 E.; Berendsen, H. J. C. *J. Comput. Chem.* **2005**, 26, 1701–1718.
- 1161 (76) Kritzer, J. A.; Tirado-Rives, J.; Hart, S. A.; Lear, J. D.; Jorgensen,  
1162 W. L.; Schepartz, A. *J. Am. Chem. Soc.* **2005**, 127, 167–178.
- 1163 (77) Hess, B.; Bekker, H.; Berendsen, H. J. C.; Fraaije, J. G. E. M. *J.*  
1164 *Comput. Chem.* **1997**, 18, 1463–1472.
- 1165 (78) Bussi, G.; Donadio, D.; Parrinello, M. *J. Chem. Phys.* **2007**, 126,  
1166 014101.
- 1167 (79) Darden, T.; York, D.; Pedersen, L. *J. Chem. Phys.* **1993**, 98,  
1168 10089–10092.